ACS **APPLIED**
NANO MATERIALS Cite This: *ACS Appl. Nano Mater.* 2018, 1, 4306−4316

Article

www.acsanm.org

Evaluating the Critical Roles of Precursor Nature and Water Content When Tailoring Magnetic Nanoparticles for Specific Applications

Geoffrey Cotin,[†,‡] Céline Kiefer,[†,‡] Francis Perton,[†,‡] Mauro Boero,[†,‡] Burak Özdamar,[§] Assil Bouzid,[∥] Guido Ori,[†,‡] Carlo Massobrio,[†,‡] Dominique Begin,[⊥] Benoit Pichon,[†,‡] Damien Mertz,[†,‡] and Sylvie Begin-Colin*,[†,‡]

[†]Institut de Physique et Chimie des Matériaux de Strasbourg, Université de Strasbourg, CNRS, UMR 7504, F-67034 Strasbourg, France

[‡]Labex CSC, Fondation IcFRC/Université de Strasbourg, 8 allée Gaspard Monge BP 70028, F-67083 Strasbourg Cedex, France

[§]Materials Science and Engineering, Izmir Institut of Technology, 35430 Urla, Izmir, Turkey

[∥]Chaire de Simulation à l'Echelle Atomique, Ecole Polytechnique Fédérale de Lausanne, CH-1015 Lausanne, Switzerland

[⊥]Institut de Chimie et Procédés pour l'Energie, Université de Strasbourg, CNRS, l'Environnement et la Santé, UMR 7515, F-67087 Strasbourg, France

Ⓢ *Supporting Information*

ABSTRACT: Because of the broad range of application of iron oxide nanoparticles (NPs), the control of their size and shape on demand remains a great challenge, as these parameters are of upmost importance to provide NPs with magnetic properties tailored to the targeted application. One promising synthesis process to tune their size and shape is the thermal decomposition one, for which a lot of parameters were investigated. But two crucial issues were scarcely addressed: the precursor's nature and water content. Two *in house* iron stearates with two or three stearate chains were synthesized, dehydrated, and then tested in standard synthesis conditions of spherical and cubic NPs. Investigations combined with modeling showed that the precursor's nature and hydration rate strongly affect the thermal decomposition kinetics and yields, which, in turn, influence the NP size. The cubic shape depends on the decomposition kinetics but also crucially on the water content. A microscopic insight was provided by first-principles simulation showing an iron reduction along the reaction pathway and a participation of water molecules to the building unit formation.

KEYWORDS: iron oxide, thermal decomposition, iron precursor, hydration rate, synthesis mechanism, modeling
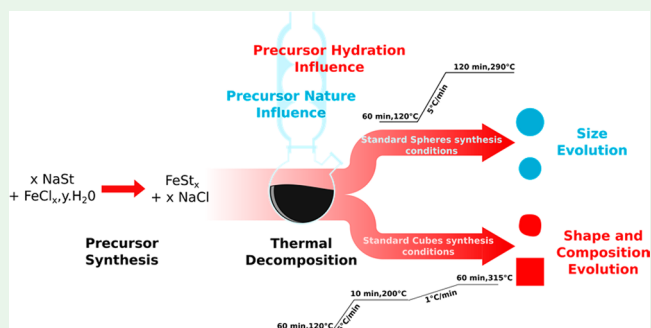
Magnetic iron oxide nanoparticles (NPs) are receiving increasing attention worldwide in view of their intrinsic properties stemming from their size, shape, and composition. This, in turn, discloses a broad range of applications, including magnetic fluids, data storage nanodevices, catalysis, and biomedical applications.[1−5] Depending on the targeted application, the NPs magnetic properties must be specifically adapted and impose strict constraints in the design of NPs with given size, composition, and shape. In the specific case of biomedical applications: to use them as T2 contrast agents for magnetic resonance imaging (MRI), iron oxide-based NPs should exhibit a high saturation magnetization (Ms) and be functionalized with ligands ensuring optimal diffusion of water molecules around the magnetic core.[6] For the treatment of cancer by magnetic hyperthermia, the amount of heat generated by NPs strongly depends on their size distribution and on their magnetic properties (high Ms and high magnetocrystalline anisotropy).[6] Given the increasing clinical importance of the benefit demonstrated by magnetic hyper-

thermia treatments,[9−13] the need for the synthesis of NPs with better performance becomes evident. By tuning the NPs shape, for example, via the synthesis of cubic iron oxide NPs or flower-shaped nanostructures enabling cooperative magnetism, the heating power of these NPs can be greatly improved.[14−19] In our case, we already demonstrated that iron oxide NPs with a diameter of ∼10 nm synthesized by a thermal decomposition process and coated with dendron molecules are very promising for in vivo diagnostic by MRI.[7,8] Dendronized nanocubes also synthesized by this process[20] were shown promising for magnetic hyperthermia even at low concentration.[19]

To envision complete in vivo biomedical developments of such designed iron oxide NPs and, in particular, of these dendronized NPs, reproducible synthesis protocols with well-

tailored reactants and high yield need to be established. Indeed, NPs shape control remains difficult to achieve, and experimental results from NPs systems vary significantly.[14,19−23] This issue underscores the need to identify reproducible tunable synthesis methods that allow the design of NPs possessing the desired structural parameters and the required physical-chemical properties.

Among all the viable synthesis methods,[24−32] the thermal decomposition method has been shown to be particularly very promising to tailor the size[22,33−35] and the shape[20,36,37] of NPs. This specific process is based on the thermal decomposition of a metal precursor in a high boiling point organic solvent in the presence of surfactants. Among these thermal decomposition approaches, the most used wordwilde are those developed by Hyeon[33] and Sun,[34] involving mainly iron oleate and iron acetyl acetonate, respectively, as iron precursors. However, the actual mechanism along which the synthesis proceeds is still not well understood, which prevents a relevant understanding of structure-size-composition-shape-properties relationships in NPs. For instance, in the specific case of cubic-shaped NPs, the most used method is the one proposed by Kovalenko[36] based on the decomposition of iron oleate in the presence of a mixture of oleic acid and sodium oleate. The sodium oleate is expected to strongly bind on specific surfaces of nuclei (i.e., initial NPs' seeds) and to promote a cubic growth. An appropriate calibration of both the heating rate and the boiling point of the organic solvents allows controlling the nanocube size. Former works have reported that such nanocubes are not homogeneous in composition and consist in core−shell nanocubes with a core constituted of the wüstite FeO phase and a shell of $Fe_{3−x}O_4$.[36,38] Pellegrino and co-workers deepened the analysis of the nanocube synthesis by investigating the thermal decomposition of iron acetyl acetonate and decanoic acid in dibenzylether.[14] They were able to show that, by changing the amount of dibenzylether by introducing squalene, the nanocube shape was achieved because of the decomposition products of dibenzylether during the synthesis, which can be adsorbed on specific faces, thus triggering the desired cubic growth.[23]

In view of the high potential of this class of synthesis methods, a fine control of the thermal decomposition becomes a primary issue for a tunable and a reproducible NPs synthesis and design. To date the most accredited model able to rationalize this synthesis process is the one proposed by LaMer and Dinegar.[25,39−42] Specifically, [polyironoxo clusters] monomers,[42] the minimum building blocks, are generated upon thermal decomposition of the precursors. Then, when the monomer concentration exceeds a given limit, the nucleation process can occur with a number of nuclei depending on the excess in monomer concentration with respect to the concentration limit. Clearly, upon nucleation, at a given point, the monomer concentration decreases below this concentration limit, and if some monomers are still available in the environment, a grain growth is observed.

In the specific process of Hyeon et al.,[43] which involved basically the decomposition of iron oleate in the presence of oleic acid as surfactant in an organic solvent, a lot of parameters have been tuned to modulate the NPs size and shape such as the nature of organic solvent, the ratio surfactant/precursor, the nature of surfactant (carboxylic acid or amine) but without established rules. More and more studies pointed out recently a possible influence of the precursor on the size control. Indeed, it is suggested that the precursor stability would be altered during the synthesis by interacting with surfactants and/or solvents. Indeed with the widely used oleate complex[20,33,35,42−44] or with iron stearate[19,21,22,45] used in our group, the monomer formation was observed to depend on the nature of solvents and ligands and also to be reaction time- and/or temperature-dependent. These observations allow to infer that the monomer formation depends on the iron precursor stability. The chemical environment and the experimental conditions, in turn, have a direct influence on the precursor stability as evidenced by Bronstein et al.[44] who pointed out the effect of solvent and washing conditions on the iron oleate precursor thermal behavior and, ultimately, on the nucleation and germination processes. Hufschmid et al.[46] also demonstrated that a nature of precursor will be more suited for the synthesis of an NP with specific size range.

In addition, by using the iron oleate precursor, we were able to synthesize spherical NPs with different sizes[35] and rather regular nanocubes with straight faces and a good monodispersity by resorting to the Kovalenko's method,[20,36] (Figure S1) but iron oleate batches were observed to be unstable with time, and from one batch to another one, different sized/shaped NPs may be obtained, thus jeopardizing the synthesis' reproducibility. On the basis of these experiments with iron oleate synthesized in our laboratory[20,33] and by considering the low stability of this iron complex, which is highly sensitive to the synthesis, washing, and storing conditions,[20,44] a commercial iron stearate complex bearing two stearate chains was used. A synthesis in standard conditions for spherical NPs has shown a reproducible synthesis of 10 nm NPs.[22] However, the replacement of iron oleate with iron stearate in the synthesis conditions of nanocubes (which consist just in replacing one part of oleic acid by sodium oleate) led to nanocubes of lower quality (very deformed; Figure S1) than those obtained with the good batch of iron oleate.[20] In addition, a change in the batch of commercial iron stearate was shown to lead to nanocubes in the synthesis conditions of 10 nm nanospheres (Figure S2). After evidencing the presence of impurities in commercial batches, we decided to synthesize our own iron stearate. Our own compound was shown to be more stable with time and to allow for a reproducible synthesis of spherical NPs with a mean size of 10 nm. However, high-quality nanocubes were always difficult to obtain evidencing an unresolved issue in the nanocube synthesis mechanism.

We decided thus to prepare two *in house* iron stearates (one iron stearate that would bear two stearate chains as the commercial iron stearate and the second one that would bear three stearate chains as the iron oleate precursor) and to investigate the effect of their nature (two or three stearate chains) and hydration conditions on the formation and composition of spherical and cubic-shaped NPs (Scheme 1). We used well-established synthesis protocols of spherical NPs with a mean size of 10 nm[22] and of nanocubes[19,20] to investigate only the precursor effect. To date, very few works dealt with the influence of the iron precursor structure on the synthesis of NPs.[44,47,48] Experiments have been complemented by dynamical simulations within a first-principles framework enriched by free energy sampling techniques. These studies,[49] extended in the present work, allow to inspect the thermal decomposition reaction pathways and to unravel the role of water in triggering the reaction. This provides hints for a better control of the process and thus for the NPs design.

Scheme 1. Schematic of NPs Synthesis Investigation
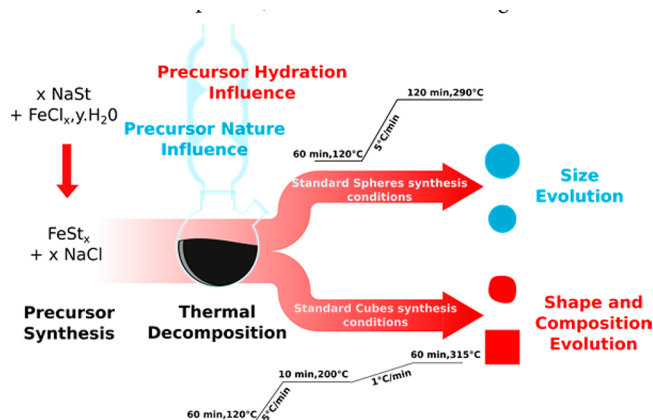
■ EXPERIMENTAL DETAILS

Iron Precursors Synthesis. Iron stearate (II) and (III) were prepared by precipitation of sodium stearate (98.8% TCI) and ferrous chloride (99%, Acros Organic) or ferric chloride (99%, Sigma) salts in an aqueous solution. Briefly, sodium stearate (9.8 g, 32 mmol) was transferred into a two-necked to a round-bottomed flask (RBF) and solubilized in distilled H_2O (dH_2O, 80 mL). The solution is heated to reflux and stirred for 30 min until complete dissolution of the stearate. Separately, $FeCl_2 \cdot 4H_2O$ (3.16 g, 16 mmol) or $FeCl_3 \cdot H_2O$ (2.88 g, 16 mmol) was dissolved in dH_2O (40 mL) and added onto the sodium stearate solution under vigorous stirring. A light orange precipitate formed immediately. The solution is kept under stirring at this temperature 15 min. Thereafter the solution is allowed to cool to room temperature (RT). The obtained precipitate is washed once by centrifugation (hot dH_2O, 14 000 rpm, 10 min). The product is then filtrated with a Büchner funnel and oven-dried at 65 °C for 24 h. Dehydration of the precursor is performed in an oven at 140 °C for 48 h.

Standard Synthesis of 10 nm Sized NPs. Iron oxide nanospheres (NS) are synthesized from an already reported reproducible protocol,[22] which consists in the thermal decomposition of the iron stearate in the presence of oleic acid (OA, 99%, Alfa Aesar) in dioctylether (OE, 99%, Sigma). The as-synthesized iron stearate (1.38 g for $FeSt_2$ and 2 g for $FeSt_3$, 2.2 mmol in iron) is mixed with OA (1.24 g, 4.4 mmol) in 20 mL of OE in a two-neck RBF. The mixture is stirred and heated at 120 °C for 1 h without reflux condenser to dissolve the reactants and remove the volatile molecule residues. We demonstrated earlier that, if the heating step at 120 °C is suppressed, the mean size is smaller.[22] The hypothesis was that such volatile molecule residues and, in particular, water would affect the thermal stability of the iron complex.

The cooler is then connected to the flask, and the solution is heated to the boiling temperature (~290 °C) with heating rate of 5 °C/min and heated to reflux for 2 h under air. After it cooled to RT, a black suspension is obtained, which is solubilized in 10 mL of chloroform. The NPs are then precipitated by the addition of an excess of acetone the first time and washed three times with chloroform and acetone at a ratio of 1:4 at 14 000 rpm for 5 min by centrifugation. The NPs can finally be suspended in 50 mL of tetrahydrofuran (THF).

Standard Synthesis of Nanocubes. Iron oxide nanocubes (NC) are synthesized from an already reported protocol,[20,36] which consists in the thermal decomposition of the iron stearate in the presence of oleic acid and sodium oleate (NaOl, 97%, TCI). Iron stearate (2.32 mmol) is mixed with 3 mmol of ligands (OA, 0.45 g, 1.5 mmol and NaOl, 0.45 g, 1.5 mmol) in 15 mL of octadecene (OD, 90%, Alfa Aesar). The mixture is stirred and heated at 120 °C for 60 min without reflux condenser to dissolve the reactants and remove the volatile molecule residues. The cooler is then connected to the flask, and the solution is heated to 200 °C for 10 min with a heating rate of 5 °C/min. The solution is then heated to 315 °C with a heating rate of 1 °C/min and refluxed for 60 min under air. After it cooled to RT,

a black and viscous suspension is obtained and is treated as previously. The NPs can finally be suspended in 50 mL of THF.

Determination of the Synthesis Yield. After the synthesis, the NPs are washed once as described above. The supernatant is collected, and the NPs are solubilized in 5 mL of chloroform. Defined volumes of both solutions (200 μL for the NPs and 3 mL for the supernatant) are then digested for 48 h at room temperature with 220 μL of HNO_3. The iron solutions are then diluted to 10 mL in deionized water. The concentration is then measured on a PerkinElmer AAS spectrometer.

Characterization Techniques. NPs were characterized by transmission electron microscopy (TEM) with a JEOL 2100 microscope operating at 200 kV (point resolution 0.18 nm). The size distribution of NPs was calculated from the size measurements of more than 300 nanoparticles using ImageJ software.

Scanning electron microscopy (SEM) was performed using a Zeiss gemini SEM 500 microscope equipped with a field emission gun (SEM-FEG) operating at an accelerating voltage of 1 kV.

Thermogravimetric analysis (TGA) measurements were performed on dried powder samples from 20 to 600 °C at 5 °C/min under air by using an SDJ Q600 apparatus.

The X-ray diffraction (XRD) pattern was recorded at room temperature with a Bruker D8 Advance diffractometer equipped with a monochromatic copper radiation source ($K\alpha = 0.154\,056$ nm) and a Lynx-Eye detector in the 27–65°(2θ) range with a scan step of 0.03°. High-purity silicon powder ($a = 0.543\,082$ nm) was systematically used as an internal standard. Profile matching refinements were performed through the Fullprof program[50] using Le Bail's method[51] with the modified Thompson-Cox-Hasting (TCH) pseudo-Voigt profile function.

Standard infrared spectra were recorded between 4000 and 400 cm^{-1} with a Fourier transform infrared (FTIR) spectrometer, Spectrum 100 from PerkinElmer. Samples were gently ground and diluted in nonabsorbent KBr matrixes.

Computational Methods. Our simulations make use of first-principles molecular dynamics (FPMD)[52] within the density functional theory (DFT)[53] framework as implemented in the CPMD[54] code. The exchange and correlation interactions are described by the Becke and the Lee-Yang-Parr functionals (BLYP),[55,56] respectively. Core−valence interactions are accounted for via norm-conserving Troullier-Martins pseudopotentials (PPs)[57] for O, C, and H atoms constituting the ligands, and Goedecker-Teter-Hutter[58] semicore ones for the metal centers of the precursor molecules. Valence electron orbitals are represented in a plane wave (PW) basis set with a cutoff energy of 80 Ry. A spin-unrestricted approach is adopted in all the simulations, and van der Waals interactions are included according to Grimme's D2 formula.[59] This methodology has proved to be instrumental for a wealth of complex hybrid systems.[60−62] Free energy profiles for the various desorption processes have been sampled according to the Blue Moon ensemble (BME) approach.[63−65] The selected reaction coordinates are assumed to be distances between the metal center and the carboxylate group of the coordinated ligand. Further details on the computational setup have been extensively reported in ref 49.

■ RESULTS

Synthesis of Spherical Iron Oxide Nanoparticles from in-House Iron Stearate Precursors. Iron oleate as a precursor for the synthesis of iron oxide NPs by thermal decomposition is mainly synthesized by mixing a suspension of hexahydrate iron(III) chlorides in water with a suspension of sodium oleate in organic solvent, which leads to iron oleate precursor formation in the organic solvent.[33] However, Bronstein et al.[44] reported an influence of washing solvent, aging, and storage on the iron oleate stability, and we also observed in our earlier studies[20,22] an effect of washing and drying conditions. Therefore, among published synthesis methods of metal carboxylates,[66,67] a simple, scalable, and

"green" approach involving a simple coprecipitation of the iron stearate in water was chosen. As the commercial iron stearate that we used at first was "sold" as an iron(II) stearate, and as iron oleates were synthesized under iron(III) oleates, both iron(II) and iron(III) stearates were synthesized by this coprecipitation method and named $FeSt_2$ and $FeSt_3$, respectively. Hydrated iron(II or III) chlorides were used as iron precursors for the iron stearate synthesis. Iron oleate is generally synthesized from such precursors, and no differences were observed when iron stearates were synthesized from iron sulfates. The main important parameter identified was the purity of sodium stearate reactant NaSt.

Considering the influence of solvent and drying conditions on the decomposition of the iron oleate in earlier studies and the reported difficulties to obtain anhydride stearate,[66] the dehydration of both iron stearates was also investigated.

The TGA curves of both hydrated stearates $FeSt_2$ and $FeSt_3$ (Figure 1) displayed similar shapes with a first small weight
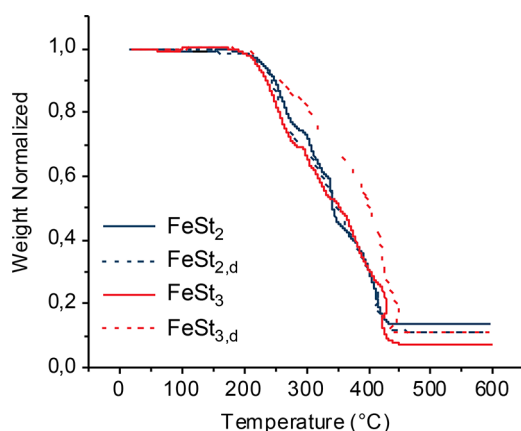

Figure 1. TGA curves of hydrated (plain line) and dehydrated (dotted line) $FeSt_2$ (blue) and $FeSt_3$ (red) iron stearates.

loss below 200 °C attributed to dehydration of powders and a second large weight loss above 200 °C attributed to the decomposition of stearates.[25,42,43] TGA experiments were performed on several iron stearate batches, and similar TGA curves were observed (Figure S3). The TGA curves (Figure 1) are also similar to that reported for iron oleate.[22,25,42] TGA or differential thermal analysis (DTA) curves were earlier shown by Heyon et al.[25,42] and Bronstein et al.[44] to provide useful information on the nucleation and growth steps.

On the basis of IR spectroscopy and TGA/differential scanning calorimetry (DSC) analyses, it was inferred by Heyon et al. that, in the first step above 200 °C, one oleate ligand dissociated from the iron oleate precursor in the temperature range of 200−240 °C, and the other two oleate moieties dissociated at ~300∘C following a CO_2 elimination pathway.[42]

From TGA curves of both iron stearates and from dehydration experiments at different temperatures by checking the IR spectra of iron stearates at each step, a dehydration treatment was established at 140 °C for 48 h. Dehydration experiments are generally conducted by heating powders up to 200 °C, but heating treatments above 140 °C or too long at 140 °C have been shown to induce not only dehydration but also to affect the iron stearate structure (Figure S4). As observed by infrared spectroscopy, the IR bands (especially in the range of 1730−720 cm^{-1}) strongly evolved after heat treatment above 140 °C (Figure S4). This treatment led to a

mean weight loss of 20 and 12% for $FeSt_3$ and $FeSt_2$, respectively, suggesting a higher hydration rate of $FeSt_3$ by comparison to $FeSt_2$. The dehydrated powders are named $FeSt_{2,d}$ and $FeSt_{3,d}$.

All iron stearates were then tested in standard conditions leading to the reproducible synthesis of 10 nm NPs (thermal decomposition of the commercial iron(II) stearate in the presence of oleic acid in octylether[22]). Iron oxide NPs with a spherical shape were reproducibly synthesized with all stearates, and representative TEM images of the different syntheses are given in Figure 2. The mean NPs size with $FeSt_3$,
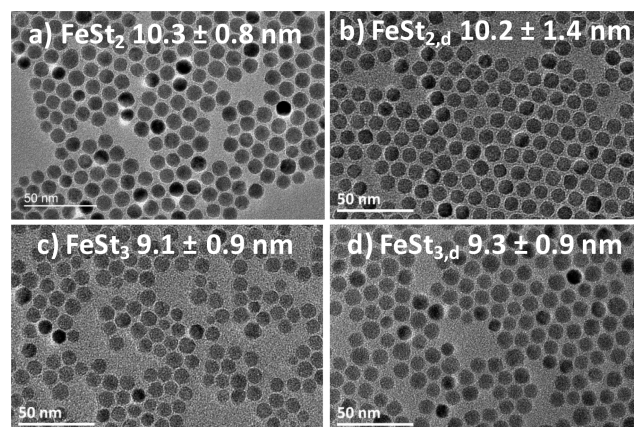

Figure 2. Standard synthesis of 10 nm sized NPs with iron(II) (a) and (III) (c) stearates and dehydrated iron(II) (b) and (III) (d) stearates.

whatever its hydration state, is slightly smaller than that obtained with $FeSt_2$ and $FeSt_{2,d}$ (Table 1). XRD measurements (Figure S5) confirmed the composition of NPs, which consist as expected in a spinel structure $Fe_{3-x}O_4$ with a lattice parameter of 8.379 ± 0.001 Å in agreement with published results.[22,35,68]

The nature of the iron stearate has also an influence on the synthesis yield. The NPs yield is very high for all iron stearates, but it is higher with iron(II) than with iron(III) stearate, and the dehydration step allowed improving this yield (Table 1). The effect of the precursor nature on the yield was also confirmed by a two-step synthesis process with iron stearates: the NPs synthesis at ~290 °C was performed once, and after it cooled to 100 °C, the synthesis step (without adding reactants and by just applying the heating ramp) was reproduced again. During the second synthesis step, the remaining precursors may contribute to the growth of NP synthesized during the first step. From Figure S6 and Table 1, a clear correlation is noticed between the mean size of NPs after these two synthesis steps and the yields. An increase of the NPs mean size after the two-step process is observed with $FeSt_2$ (lower yield) by comparison with dehydrated $FeSt_2$ (slightly higher yield). Considering the standard deviation on the mean size and earlier results on the reprocibility of the 10 nm NPs synthesis and the observed size variation,[22] one may consider that no size variation occurs with $FeSt_{2,d}$. With $FeSt_3$, only the dehydrated one led to a slight increase in the NPs size. That confirmed that $FeSt_2$, whatever its hydration rate, better decomposed than $FeSt_3$ below 290 °C.

Of particular note is the fact that, after the first synthesis step in the two-step synthesis process, the NPs size is smaller than that after only one synthesis step. We also observed such

Table 1. TEM Mean Size and Yield for Nanoparticles Synthesized in Standard Synthesis Conditions of 10 nm Sized NPs and Shape and TEM Mean Size for Nanoparticles Synthesized in Standard Conditions of Nanocubes as a Function of the Nature of Stearates

		$FeSt_2$	$FeSt_{2,d}$	$FeSt_3$	$FeSt_{3,d}$
standard 10 nm synthesis	TEM mean size (nm)	10.3 ± 0.8	10.2 ± 0.9	9.1 ± 0.9	9.3 ± 0.9
	yield (%)	90	94	83	85
	two synthesis steps (nm)	9.6 ± 1.2	9.5 ± 0.9	8.4 ± 0.4	8.3 ± 1
		11 ± 1.1	9.2 ± 1.1	8.3 ± 1.2	8.8 ± 1
standard nanocubes synthesis	shape	not defined shape	quite cubic	not defined shape	quite cubic
	TEM mean size (nm)	13.5 ± 1.8	10 ± 0.6	8.3 ± 2.2	15.9 ± 1.8

smaller size during a seed-mediated growth process to grow a CoO layer at the surface of iron oxide nanoparticles (IONPS).[22,69] We supposed that some growth should occur during the whole cooling stage.

The NPs size (from standard 10 nm sized NPs synthesis) and yield were thus shown to be higher with $FeSt_2$ than with $FeSt_3$, whatever their hydration state, and the dehydration would favor the decomposition of precursors. The synthesis yield and the two-step syntheses suggested that most of $FeSt_2$ precursors were decomposed (and formed monomers) in this synthesis condition below ~290 °C, whereas all $FeSt_3$ precursors were not decomposed. With $FeSt_3$, some other $FeSt_3$-based precursors thermally more stable should be present in the reaction mixture and would decompose only above 290 °C when most of $FeSt_2$-based precursors would be decomposed below 290 °C. Therefore, the higher size of NPs after the two-step synthesis process with $FeSt_2$ is due to its kinetics of decomposition; $FeSt_2$ decomposed below 290 °C, but it required longer time than the 2 h to be fully decomposed.[22] Therefore, the second synthesis step allowed continuing the decomposition of precursor and contributed to the further growth of NPs. With the $FeSt_3$ precursor, there is no further growth, as the growth is not limited here by the kinetics but by the decomposition temperature of $FeSt_3$.

Indeed, it has often been reported that the size of NPs depends on the boiling point of solvents, and the higher the boiling point and the larger is the mean size.[22,40,43,44] That was attributed to the decomposition of iron precursor on a large range of temperature due to the presence in the reacting media of several types of precursors with different thermal stability. The starting iron precursor has often been suggested to react with the surfactants such as oleic acid or solvent to form other precursors with different thermal stability. Such hypothesis is confirmed here by considering the differential thermogravimetry (DTG) curves (derivative of TGA curves) of stearates, which clearly evidenced different thermal behaviors.

The study of DTG (Figure 3) and DTA curves (Figures S7 and S8) evidenced four main weight loss steps as already reported, but several DTG peaks may be observed for some steps: areas III and IV in Figure 3.

The last step (area IV in Figure 3 and Figures S7 and S8) does not occur in the thermal decomposition process, which is mostly conducted below 350 °C. This step with a peak at ~420 °C for $FeSt_2$ and 450 °C for $FeSt_3$, which presented also an additional weight loss before this peak at 420 °C, is related to an exothermic peak in DTA curves (Figures S7 and S8) and corresponds to a sudden decomposition of a product. It is attributed to CO_2 departure. Indeed the decomposition of iron alkanoates has been largely investigated and is known to lead to the formation of ketones and CO_2.[44,67] Such decomposition and formation of CO_2 were also confirmed by IR spectroscopy
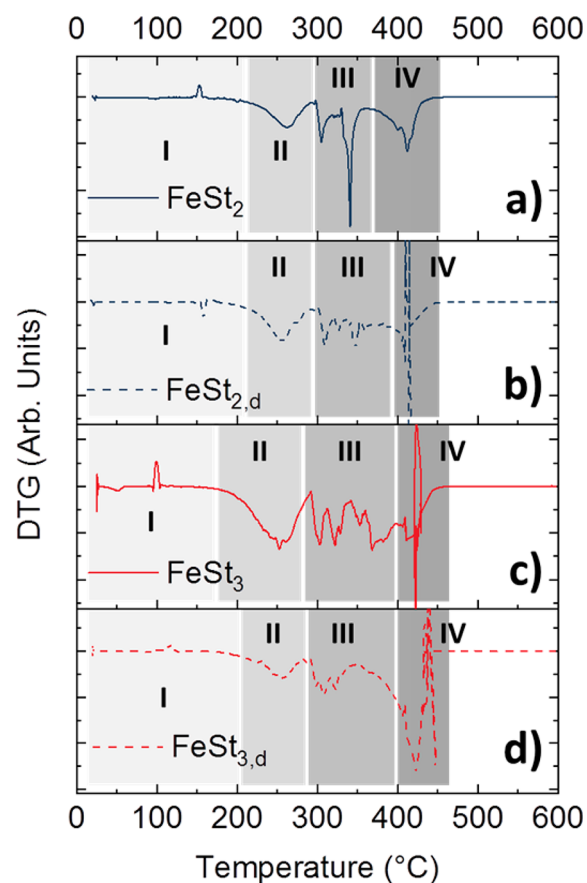

Figure 3. DTG curves of iron(II) (a) and (III) (b) stearates and dehydrated iron(II) (c) and (III) (d) stearates.

coupled with mass spectroscopy as a function of temperature (to be published).

The first weight loss (area I in Figure 3) is attributed to dehydration of iron stearates. From earlier studies, the second weight loss range (area II in Figure 3 and in Figures S7 and S8) would correspond to the first iron stearate decomposition step leading to sufficient monomer for the germination step.[22,33,34,42,43] Hyeon et al. and Know et al. have identified the germination step in this temperature range as well as Bronstein et al.,[44] who have also investigated the thermal decomposition of iron oleates by TGA and DTA. They observed four main DTA peaks, one corresponding to solvent evaporation, one around 240 °C corresponding to the germination, one around 300 °C attributed to the growth step, and the last one above 400 °C due to decomposition of organic molecules. Therefore, from these considerations, one may conclude that all stearates induced a germination at

similar temperatures exhibiting a DTG peak around 240−250 °C (area II in Figure 3).

The main difference in thermal behavior between the different precursors is found between 290° and 400 °C in area III (Figure 3), which corresponds to the growth step from previous studies.[42−44] The area III in Figure 3 is thus ascribed to the decomposition range of precursors contributing to the NPs growth. Several peaks are observed in this area depending on the iron stearates. This peak distribution should be due to the presence of a distribution of iron stearates with different chemical stabilities.

One may notice that the last peak is observed below 350 °C for $FeSt_2$ and $FeSt_{2,d}$ when it is at higher temperature for $FeSt_3$ and $FeSt_{3,d}$. That suggested that the decomposition is quite finished at maximum 340 °C (all the monomers have been generated) for $FeSt_2$ and $FeSt_{2,d}$, when a higher temperature (at minimum 380 °C) needs to be reached to induce the decomposition of all different stearates in $FeSt_3$ and $FeSt_{3,d}$. After dehydration, the distribution of precursors seems less broadened, although some decomposition is observed up to 380 °C for $FeSt_{3,d}$. These conclusions explained the results observed during the NPs synthesis with all stearates: the lower decomposition yield of $FeSt_3$ and $FeSt_{3,d}$ by comparison with that of $FeSt_2$ and $FeSt_{2,d}$ is explained by the NPs synthesis temperature at ∼290 °C, which allowed decomposing most of the iron precursors in $FeSt_2$ and $FeSt_{2,d}$ when a higher temperature would have been necessary to decompose all precursors in $FeSt_3$ and $FeSt_{3,d}$.

These results demonstrate that $FeSt_2$ "better" decomposed in the synthesis conditions below 290 °C than $FeSt_3$ and that the dehydration favored the decomposition of stearates below 290 °C. It explains the lower mean size of NPs synthesized with $FeSt_3$: the amount of produced monomer is lower, and thus the nucleation and grain growth is more limited. At this point, assuming that $FeSt_3$ would have one stearate more than $FeSt_2$, after the nucleation step that is reported to occur in the same temperature range between 200 and 240 °C by loss of one stearate chain, the further decomposition of $FeSt_2$ may be considered as easier than that of $FeSt_3$, which would bear one more stearate chain. The lower yield with $FeSt_3$ may be thus related to the decomposition kinetics, which would be faster and occur at lower temperature with $FeSt_2$ than with $FeSt_3$. Water is observed also to affect this decomposition kinetics, as dehydrated iron stearate decomposed "more" than the hydrated one. That is also confirmed by modeling as described below.

Dynamic Simulations. Dynamical simulations on either dry or hydrated $FeSt_2$ were performed to investigate the role of hydrating H_2O molecules on the decomposition mechanism of the precursor. A first set of FPMD runs at finite temperature ($T = 300$ K and $T = 500$ K) to equilibrate the system prior to BME simulations allowed also to assess the stability of the stearates, which upon standard geometry optimizations reached the stable configurations shown in Figure 4.

Since the central Fe atom is fourfold coordinated with O atoms belonging to the −COO moieties of the ligands, and this coordination being planar, two additional coordination sites are, in principle, available to complete the hydration shell of Fe, one above this coordination plane and one below (Figure 4, bottom panel). In dry conditions, the iron atom is found to be in an Fe^{2+} oxidation state, whereas in the case of two-molecule hydration an Fe^{3+} is realized, as confirmed by a Bader charge analysis.[49,70] More precisely, the values of the
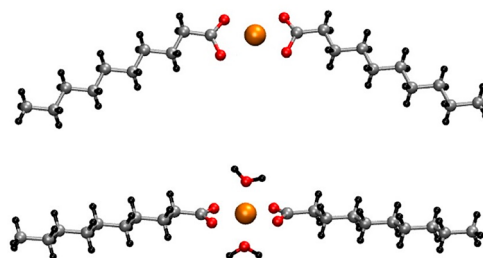

Figure 4. Equilibrium geometries of $FeSt_2$ in the absence of hydrating water (top) and microsolvation conditions with one or two water molecules (down). In case of partial hydration one of the two H_2O molecules is absent. Fe, O, C, and H atoms are shown as orange, red, gray, and black balls, respectively.

Bader charges are +1.8 for the dry planar configuration and +2.8 or +2.6 for the full (two H_2O molecules) and partial (one H_2O molecule) hydration conditions, respectively. However, at finite temperature, this situation changes significantly, and Fe^{3+} reduces to Fe^{2+}. The reasons for this reduction processes are deeply different for the two cases of partial (one H_2O molecule) and full (two H_2O molecules). In the first one, the water molecule is simply released from the solvation shell of the metal center, and the $FeSt_2$ reverts back to the dry conformation of Figure 4. Instead, in the case of complete hydration, the two H_2O molecules coordinated to the metal center displace between the ligand and the Fe site. They realize a planar configuration in which one proton of the water molecules becomes a shared H^+ shifting continuously between an O atom of the −COO group and the H_2O molecule (Figure 5)[49] as in a sort of incompletely hydrogen-bond connected Zundel complex.[71]
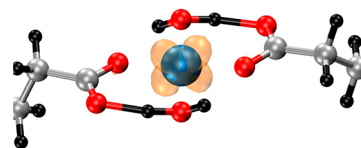

Figure 5. Equilibrium geometry of $FeSt_2$ around the metal center at 300 K in the presence of water. The color code is identical to the one of Figure 5 apart from the Fe cation colored in blue. The spin density of the Fe^{2+} metal center is shown as an orange isosurface at a value of $\pm 1 \times 10^{-2}$ e/Å^3.

Since relatively large activation barriers exist for the thermal decomposition of the $FeSt_2$, we resort to BME simulations to inspect the reaction pathway. Details about these simulations have been reported elsewhere.[49] Here we limit our analysis to the results strictly necessary to the ongoing discussion. Specifically, in dehydrated conditions, the departure of one ligand is accompanied by a temporary transition from Fe^{2+} to Fe^{3+} conditions, this meaning that one of the two O atoms of the carboxylate group of the departing ligand remains in the coordination shell of Fe, whereas the other one starts pulling apart (Figure 6). Nonetheless, this change in the oxidation state is only temporary and the first step toward the formation of the Fe−O seed, this O being bound to the metal one of the oxygen atoms of the St chain.

An entirely different scenario is realized in the case of complete hydration of the $FeSt_2$, which marks the start of the whole process from a configuration of the type shown in Figure 6. In this case, by contrast to the dehydrated iron stearate, no
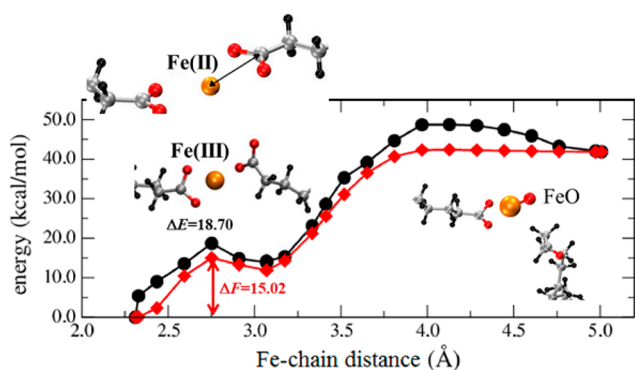
Figure 6. Free (red) and total (black) energy profiles along the reaction pathway for the dissociation process of dry $FeSt_2$. The snapshots show the main phases of the reaction mechanism.

transient oxidations states from Fe^{2+} to Fe^{3+} could be observed. Instead, the Zundel complex evolves into a complete dissociation of water molecules into a proton H and a hydroxyl anion OH^-. The former binds to the −COO group of the St ligand, whereas the second goes forming an Fe−OH building block that can become Fe−O upon dehydrogenation, as specified in ref 49. However, this H-removal process escapes any possible control and, although the activation barrier lowers considerably, the presence of an extra H in the iron oxide building block can have a negative effect on the assembly of nanoparticles. This process is summarized in Figure 7.
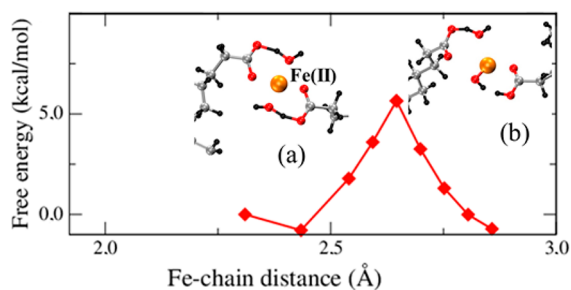

Figure 7. Free energy profiles and main phases of the reaction mechanism along the reaction pathway for the dissociation process of hydrated $FeSt_2$.

The major effect resulting from the presence of the hydrating water molecules is their active participation to the reaction mechanism. In fact, the dissociation of H_2O into H^+ and OH^- greatly facilitates the formation of the meta oxide by lowering considerably the free energy barrier for the formation of the Fe−O chemical bond, as summarized in Figures 7 and 8 and in Table 2. From a microscopic point of view, the change in the mechanism is deeply different. While in dry conditions an O atom of the St ligand must be provided to Fe, thus involving the cleavage of a C−O bond in the St chain and the formation of a new Fe−O bond, in hydrated condition the O atom of the Fe−O oxide block is provided by water. The St ligand does not undergo any bond cleavage but uptakes the proton released during the dissociation of the H_2O molecule in a rather smooth way passing across the formation of a Zundel complex. This is a common feature in any water environment[71] and, as such, realizable with a negligible activation barrier.

The molecular modeling can thus provide a clear insight into the role of water in the stabilization of iron stearate and allows
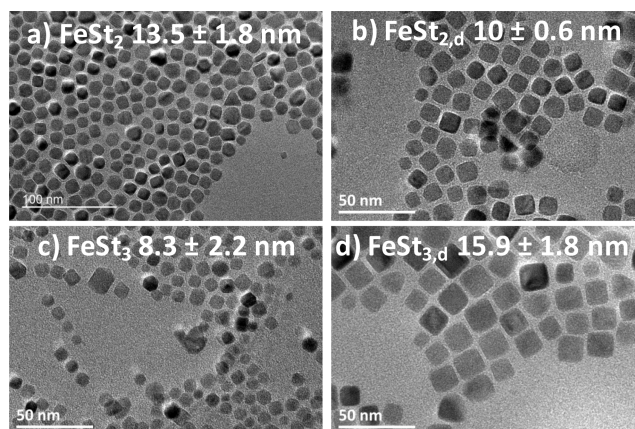

Figure 8. Standard synthesis of cubic-shaped NPs with iron(II) (a) and (III) (c) stearates and dehydrated iron(II) (b) and (III) (d) stearates.

Table 2. Free Energy Barriers for the Formation of the Intermediate Metastable Structure (if any) and the Final Dissociation Process for FeSt in Different Hydration Conditions[a]

FeSt hydration	free energy barrier for Fe^{2+}/Fe^{3+}	free energy barrier for dissociation
dry FeSt	15.02	42.10
$FeSt_2 + H_2O$	18.68	43.05
$FeSt_2 + 2\ H_2O$	0 (Zundel complex)	5.65

[a]Energies are in kilocalories per mole.

rationalizing the different behavior experimentally observed between hydrated and dehydrated samples. Indeed the dynamic simulation showed that the decomposition mechanism of iron stearate is different depending on the hydration degree of the iron stearate with the formation of either an Fe−O or Fe−OH buiding unit as a function of the hydration degree of stearates. Therefore it contributes to the explanation of the kinetics of decomposition of stearates as function of their hydration degree: with less hydrated $FeSt_2$, Fe−O units are directly formed when with hydrated iron stearates, there is the formation of Fe−OH, which needs further to be decomposed to form Fe−O. The formation of Fe−OH units would also explain that the decomposition of hydrated stearates requires higher temperatures to lead to Fe−O bonds.

Synthesis of Cubic-Shaped Iron Oxide Nanoparticles from in-House Iron Stearate Precursors. The standard synthesis conditions of iron oxide nanocubes,[20] which were shown to conduct to regular nanocubes with straight faces (when the iron oleate batch was considered as "optimal"), were also tested with these iron stearates. As observed in Figure 8, without dehydration, the cubic morphology can not be obtained. Nanocubes with higher shape quality were synthesized with dehydrated iron stearates. Thus, the dehydration of iron stearate precursor appeared as very important to control the shape of NPs. This is in agreement with our empirical experimental observation that the dehydration time of iron oleate on $MgSO_4$ was one parameter crucial to obtain iron oleate precursor suitable for the nanocube synthesis.[72] Both nanocube synthesis led to core−shell $Fe_xO@Fe_3O_4$ composition as confirmed by XRD measurement (Figure S5). Lattice parameters calculated from Rietveld refinement gave a parameter of 8.392 ± 1 Å for the

shell close to that of stoichiometric magnetite (0.8396 nm, JCPDS file 19-629) and of 4.237 ± 1 Å characteristic of an Fe_xO wüstite core. Such a core−shell composition was also reported when using the oleate precursor.[20]

Thus, we did not succeed in synthesizing nanocubes with *in house* and commercial iron stearates because they were more hydrated whatever their synthesis conditions (coprecipitation in water or biphasic synthesis) than the iron oleate obtained mainly by biphasic approach. That may be explained by the fact that iron oleate is generally obtained as an oily product when iron stearates, whatever their origin: whether commercial or *in house,* they are under the form of powder. The stearates will be always more hydrated than iron oleate due to their synthesis by coprecipitation in water. To form the nanocubes, sodium oleate is added to the reactants mixture in replacement of a part of the surfactant to adsorb on specific faces of iron oxide seeds and then to drive the growth toward a cubic morphology. The high ability of sodium oleate to form micelles[73] at low water concentration in organic solvent would explain the difficulty to obtain nanocubes with *in house* and commercial iron stearate, which are hydrated. Sodium oleate is involved in micelles, and thus not enough sodium oleate is available to favor a perfect cubic growth. Nevertheless, the decomposition kinetics should also be important. After dehydration, the distribution of precursors seems less broadened. After the germination step at ~250 °C (area II in Figure 3), the weight loss (area III in Figure 3) is higher suggesting a faster monomer formation kinetics in agreement with modeling experiments. Thus, dehydrated iron stearates would favor a higher growth kinetics. Nevertheless, the nanocube size is higher with $FeSt_{3,d}$ than $FeSt_{2,d}$, which decomposed faster at lower temperature. That would be in agreement with the fact that smaller nanocube sizes are generally obtained when applying high heating rates.[20,36]

Influence of Aging on $FeSt_2$. As the iron oleate precursor was observed to be altered with aging and storage conditions, the stability of $FeSt_2$ has been investigated as a function of aging time. It has been stored in a vial in a desiccator under air. Then it was decomposed in a standard synthesis of 10 nm NPs at different aging times. The NPs size was found to be similar after one month, but after six months, the mean size decreased by 1 nm and by 1.5 nm finally after one year (Table 3). The

Table 3. Mean Size of NPs Synthesized Each Month for One Year with the Same $FeSt_2$ Stored up to 12 Months

months	0	1	6	12
mean size (nm)	9.7 ± 0.85	$9,6 \pm 0.9$	$8,5 \pm 1.0$	8.2 ± 1.1

aging time of the stearate has then a slight influence on the size of the NPs. Indeed, the storage conditions were not strict, and a hydration of iron stearate has occurred with time leading to lower NPs size. A storage under vacuum or inert gas should allow a longer storage quality of the precursor. Still up to one month, "simple" storage conditions can be used.

These results also demonstrated that, from the point of view of the synthesis of precursor at low price, $FeSt_2$ may be used for the standard synthesis of 10 nm NPs. For a tuning of the shape, dehydrated iron stearates appear more suitable leading to more defined nanocubes, and the cubic shape with iron(III) stearate appeared more defined than iron(II) stearate. That may be related to the fact that iron(III) stearate bore more

chelating ligands than iron(II) stearate contributing thus to the cubic growth.

CONCLUSION

Two $FeSt_2$ and $FeSt_3$ iron stearate precursors have been synthesized by coprecipitation technique and dehydrated. Then they have been used to synthesize spherical 10 nm NPs and nanocubes following standard procedures established earlier using commercial $FeSt_2$ iron stearate and *in house* iron oleate.

$FeSt_2$ precursors were shown to produce spherical NPs with a slightly higher mean diameter and with a higher yield than $FeSt_3$. The dehydration of these stearates was shown to induce a slight increase in the spherical NPs diameter and yield. From thermal analyses and modeling, it was demonstrated that hydrated and dehydrated $FeSt_2$ is fully decomposed at a lower temperature than $FeSt_3$ and that the dehydration favors the decomposition of stearates. The yield and the final mean size of spherical NPs are thus clearly related not only to the nature of iron stearates $FeSt_2$ or $FeSt_3$, which induce the presence of iron stearates with different thermal stabilities, but also to their hydration rate, as the dehydration led to an increase in the decomposition kinetics. Modeling further showed that the dehydration caused by the temperature induced the departure of a water molecule along with the reduction of Fe^{3+} in Fe^{2+}. Thus, when water molecules are strongly bounded to iron atoms, they are responsible for the intermediate formation of Fe−OH building units requiring higher temperature in the iron oxide NPs formation process.

Finally, the formation of nanocubes required dehydrated iron stearates, which may be explained by their higher decomposition kinetics and by the fact that sodium oleate in the presence of water formed micelles preventing this ligand to play its role of shape control.

To better understand the differences between stearates and the effect of the hydration state, the structures of all stearates are currently further investigated by combining different characterization, experimental, and modeling techniques.

ASSOCIATED CONTENT

Ⓢ Supporting Information

The Supporting Information is available free of charge on the ACS Publications website at DOI: 10.1021/acsanm.8b01123.

TEM images of NPs synthesized by thermal decomposition using the nanocubes protocol and the following iron precursors: (a) an iron oleate and (b) a commercial iron stearate, TEM images of NPs synthesized by thermal decomposition using the nanospheres protocol and a commercial iron stearate containing impurities, TGA curves of different samples of hydrated iron stearates, infrared spectra of $FeSt_2$ after thermal treatment at different temperatures. Alkyls bands are located in the high-frequency region of 3000−2800 cm^{-1}, HRTEM and Rietveld refinements for the spheres and cubes, TEM images of NPs after the two-step synthesis process as a function of the nature of stearates, DTA curves of the four iron stearates, and superposition of TGA, DTG, and DTA curves of four iron stearates (PDF)

■ AUTHOR INFORMATION

Corresponding Author
*E-mail: sylvie.begin@unistra.fr.
ORCID ⦿
Mauro Boero: 0000-0002-5052-2849
Assil Bouzid: 0000-0002-9363-7240
Benoit Pichon: 0000-0003-3708-6461
Damien Mertz: 0000-0002-6745-8978
Sylvie Begin-Colin: 0000-0002-2293-2226

Author Contributions
The manuscript was written through contributions of all authors. All authors have given approval to the final version of the manuscript.

Notes
The authors declare no competing financial interest.

■ REFERENCES

(1) Tartaj, P.; Morales, M. P.; Gonzalez-Carreño, T.; Veintemillas-Verdaguer, S.; Serna, C. J. The Iron Oxides Strike Back: From Biomedical Applications to Energy Storage Devices and Photoelectrochemical Water Splitting. *Adv. Mater.* **2011**, *23* (44), 5243−5249.

(2) Zeng, H.; Black, C. T.; Sandstrom, R. L.; Rice, P. M.; Murray, C. B.; Sun, S. Magnetotransport of Magnetite Nanoparticle Arrays. *Phys. Rev. B: Condens. Matter Mater. Phys.* **2006**, *73* (2), 020402.

(3) Laurent, S.; Forge, D.; Port, M.; Roch, A.; Robic, C.; Vander Elst, L.; Muller, R. N. Magnetic Iron Oxide Nanoparticles: Synthesis, Stabilization, Vectorization, Physicochemical Characterizations, and Biological Applications. *Chem. Rev.* **2008**, *108* (6), 2064−2110.

(4) Frey, N. A.; Peng, S.; Cheng, K.; Sun, S. Magnetic Nanoparticles: Synthesis, Functionalization, and Applications in Bioimaging and Magnetic Energy Storage. *Chem. Soc. Rev.* **2009**, *38* (9), 2532−2542.

(5) Lu, A.-H.; Salabas, E. L.; Schüth, F. Magnetic Nanoparticles: Synthesis, Protection, Functionalization, and Application. *Angew. Chem., Int. Ed.* **2007**, *46* (8), 1222−1244.

(6) Blanco-Andujar, C.; Walter, A.; Cotin, G.; Bordeianu, C.; Mertz, D.; Felder-Flesch, D.; Begin-Colin, S. Design of Iron Oxide-Based Nanoparticles for MRI and Magnetic Hyperthermia. *Nanomedicine (London, U. K.)* **2016**, *11* (14), 1889−1910.

(7) Basly, B.; Popa, G.; Fleutot, S.; Pichon, B. P.; Garofalo, A.; Ghobril, C.; Billotey, C.; Berniard, A.; Bonazza, P.; Martinez, H.; Felder-Flesch, D.; Begin-Colin, S. Effect of the Nanoparticle Synthesis Method on Dendronized Iron Oxides as MRI Contrast Agents. *Dalton Trans.* **2013**, *42* (6), 2146−2157.

(8) Bordeianu, C.; Parat, A.; Piant, S.; Walter, A.; Zbaraszczuk-Affolter, C.; Meyer, F.; Begin-Colin, S.; Boutry, S.; Muller, R. N.; Jouberton, E.; Chezal, J.-M.; Labeille, B.; Cinotti, E.; Perrot, J.-L.; Miot-Noirault, E.; Laurent, S.; Felder-Flesch, D. Evaluation of the Active Targeting of Melanin Granules after Intravenous Injection of Dendronized Nanoparticles. *Mol. Pharmaceutics* **2018**, *15* (2), 536−547.

(9) Maier-Hauff, K.; Rothe, R.; Scholz, R.; Gneveckow, U.; Wust, P.; Thiesen, B.; Feussner, A.; von Deimling, A.; Waldoefner, N.; Felix, R.; Jordan, A. Intracranial Thermotherapy Using Magnetic Nanoparticles Combined with External Beam Radiotherapy: Results of a Feasibility Study on Patients with Glioblastoma Multiforme. *J. Neuro-Oncol.* **2007**, *81* (1), 53−60.

(10) Maier-Hauff, K.; Ulrich, F.; Nestler, D.; Niehoff, H.; Wust, P.; Thiesen, B.; Orawa, H.; Budach, V.; Jordan, A. Efficacy and Safety of Intratumoral Thermotherapy Using Magnetic Iron-Oxide Nanoparticles Combined with External Beam Radiotherapy on Patients with Recurrent Glioblastoma Multiforme. *J. Neuro-Oncol.* **2011**, *103* (2), 317−324.

(11) Thiesen, B.; Jordan, A. Clinical Applications of Magnetic Nanoparticles for Hyperthermia. *Int. J. Hyperthermia* **2008**, *24* (6), 467−474.

(12) Http://Www.Magforce.de/en/home.html.

(13) Goya, L. A. Cell Death Induced by AC Magnetic Fields and Magnetic Nanoparticles: Current State and Perspectives. *Int. J. Hyperthermia* **2013**, *29*, 810.

(14) Guardia, P.; Di Corato, R.; Lartigue, L.; Wilhelm, C.; Espinosa, A.; Garcia-Hernandez, M.; Gazeau, F.; Manna, L.; Pellegrino, T. Water-Soluble Iron Oxide Nanocubes with High Values of Specific Absorption Rate for Cancer Cell Hyperthermia Treatment. *ACS Nano* **2012**, *6* (4), 3080−3091.

(15) Hugounenq, P.; Levy, M.; Alloyeau, D.; Lartigue, L.; Dubois, E.; Cabuil, V.; Ricolleau, C.; Roux, S.; Wilhelm, C.; Gazeau, F.; Bazzi, R. Iron Oxide Monocrystalline Nanoflowers for Highly Efficient Magnetic Hyperthermia. *J. Phys. Chem. C* **2012**, *116* (29), 15702−15712.

(16) Gazeau, F.; Lévy, M.; Wilhelm, C. Optimizing Magnetic Nanoparticle Design for Nanothermotherapy. *Nanomedicine (London, U. K.)* **2008**, *3* (6), 831−844.

(17) Lee, J.-H.; Jang, J.; Choi, J.; Moon, S. H.; Noh, S.; Kim, J.; Kim, J.-G.; Kim, I.-S.; Park, K. I.; Cheon, J. Exchange-Coupled Magnetic Nanoparticles for Efficient Heat Induction. *Nat. Nanotechnol.* **2011**, *6* (7), 418−422.

(18) Martinez-Boubeta, C.; Simeonidis, K.; Makridis, A.; Angelakeris, M.; Iglesias, O.; Guardia, P.; Cabot, A.; Yedra, L.; Estradé, S.; Peiró, F.; Saghi, Z.; Midgley, P. A.; Conde-Leboran, I.; Serantes, D.; Baldomir, D. Learning from Nature to Improve the Heat Generation of Iron-Oxide Nanoparticles for Magnetic Hyperthermia Applications. *Sci. Rep.* **2013**, *3*, 1 DOI: 10.1038/srep01652.

(19) Walter, A.; Billotey, C.; Garofalo, A.; Ulhaq-Bouillet, C.; Lefèvre, C.; Taleb, J.; Laurent, S.; Vander Elst, L.; Muller, R. N.; Lartigue, L.; Gazeau, F.; Felder-Flesch, D.; Begin-Colin, S. Mastering the Shape and Composition of Dendronized Iron Oxide Nanoparticles To Tailor Magnetic Resonance Imaging and Hyperthermia. *Chem. Mater.* **2014**, *26* (18), 5252−5264.

(20) Pichon, B. P.; Gerber, O.; Lefevre, C.; Florea, I.; Fleutot, S.; Baaziz, W.; Pauly, M.; Ohlmann, M.; Ulhaq, C.; Ersen, O.; Pierron-Bohnes, V.; Panissod, P.; Drillon, M.; Begin-Colin, S. Microstructural and Magnetic Investigations of Wüstite-Spinel Core-Shell Cubic-Shaped Nanoparticles. *Chem. Mater.* **2011**, *23* (11), 2886−2900.

(21) Baaziz, W.; Pichon, B. P.; Liu, Y.; Grenèche, J.-M.; Ulhaq-Bouillet, C.; Terrier, E.; Bergeard, N.; Halté, V.; Boeglin, C.; Choueikani, F.; Toumi, M.; Mhiri, T.; Begin-Colin, S. Tuning of Synthesis Conditions by Thermal Decomposition toward Core−Shell $Co_xFe_{1−x}O@Co_yFe_{3−y}O_4$ and $CoFe_2O_4$ Nanoparticles with Spherical and Cubic Shapes. *Chem. Mater.* **2014**, *26* (17), 5063−5073.

(22) Baaziz, W.; Pichon, B. P.; Fleutot, S.; Liu, Y.; Lefevre, C.; Greneche, J.-M.; Toumi, M.; Mhiri, T.; Begin-Colin, S. Magnetic Iron Oxide Nanoparticles: Reproducible Tuning of the Size and Nanosized-Dependent Composition, Defects, and Spin Canting. *J. Phys. Chem. C* **2014**, *118* (7), 3795−3810.

(23) Guardia, P.; Riedinger, A.; Nitti, S.; Pugliese, G.; Marras, S.; Genovese, A.; Materia, M.; Lefevre, C.; Manna, L.; Pellegrino, T. One Pot Synthesis of Monodisperse Water Soluble Iron Oxide Nanocrystals with High Values of Specific Absorption Rate. *J. Mater. Chem. B* **2014**, *2*, 4426.

(24) Yin, Y.; Alivisatos, A. P. Colloidal Nanocrystal Synthesis and the Organic−Inorganic Interface. *Nature* **2005**, *437* (7059), 664−670.

(25) Park, J.; Joo, J.; Kwon, S. G.; Jang, Y.; Hyeon, T. Synthesis of Monodisperse Spherical Nanocrystals. *Angew. Chem., Int. Ed.* **2007**, *46* (25), 4630−4660.

(26) Cushing, B. L.; Kolesnichenko, V. L.; O'Connor, C. J. Recent Advances in the Liquid-Phase Syntheses of Inorganic Nanoparticles. *Chem. Rev.* **2004**, *104* (9), 3893−3946.

(27) de Mello Donegá, C.; Liljeroth, P.; Vanmaekelbergh, D. Physicochemical Evaluation of the Hot-Injection Method, a Synthesis Route for Monodisperse Nanocrystals. *Small* **2005**, *1* (12), 1152−1162.

(28) Reiss, P.; Protière, M.; Li, L. Core/Shell Semiconductor Nanocrystals. *Small* **2009**, *5* (2), 154−168.

(29) Burda, C.; Chen, X.; Narayanan, R.; El-Sayed, M. A. Chemistry and Properties of Nanocrystals of Different Shapes. *Chem. Rev.* **2005**, *105* (4), 1025−1102.

(30) Kumar, S.; Nann, T. Shape Control of II-VI Semiconductor Nanomaterials. *Small* **2006**, *2* (3), 316−329.

(31) Tao, A. R.; Habas, S.; Yang, P. Shape Control of Colloidal Metal Nanocrystals. *Small* **2008**, *4* (3), 310−325.

(32) Jun, Y.; Choi, J.; Cheon, J. Shape Control of Semiconductor and Metal Oxide Nanocrystals through Nonhydrolytic Colloidal Routes. *Angew. Chem., Int. Ed.* **2006**, *45* (21), 3414−3439.

(33) Park, J.; An, K.; Hwang, Y.; Park, J.-G.; Noh, H.-J.; Kim, J.-Y.; Park, J.-H.; Hwang, N.-M.; Hyeon, T. Ultra-Large-Scale Syntheses of Monodisperse Nanocrystals. *Nat. Mater.* **2004**, *3* (12), 891−895.

(34) Sun, S.; Zeng, H.; Robinson, D. B.; Raoux, S.; Rice, P. M.; Wang, S. X.; Li, G. Monodisperse MFe2O4 (M = Fe, Co, Mn) Nanoparticles. *J. Am. Chem. Soc.* **2004**, *126* (1), 273−279.

(35) Demortière, A.; Panissod, P.; Pichon, B. P.; Pourroy, G.; Guillon, D.; Donnio, B.; Bégin-Colin, S. Size-Dependent Properties of Magnetic Iron Oxide Nanocrystals. *Nanoscale* **2011**, *3* (1), 225−232.

(36) Kovalenko, M. V.; Bodnarchuk, M. I.; Lechner, R. T.; Hesser, G.; Schäffler, F.; Heiss, W. Fatty Acid Salts as Stabilizers in Size- and Shape-Controlled Nanocrystal Synthesis: The Case of Inverse Spinel Iron Oxide. *J. Am. Chem. Soc.* **2007**, *129* (20), 6352−6353.

(37) Kim, D.; Lee, N.; Park, M.; Kim, B. H.; An, K.; Hyeon, T. Synthesis of Uniform Ferrimagnetic Magnetite Nanocubes. *J. Am. Chem. Soc.* **2009**, *131* (2), 454−455.

(38) Wetterskog, E.; Tai, C.-W.; Grins, J.; Bergström, L.; Salazar-Alvarez, G. Anomalous Magnetic Properties of Nanoparticles Arising from Defect Structures: Topotaxial Oxidation of Fe$_{1−x}$OIFe$_{3−\delta}$O$_4$ CorelShell Nanocubes to Single-Phase Particles. *ACS Nano* **2013**, *7* (8), 7132−7144.

(39) LaMer, V. K.; Dinegar, R. H. Theory, Production and Mechanism of Formation of Monodispersed Hydrosols. *J. Am. Chem. Soc.* **1950**, *72* (11), 4847−4854.

(40) Kwon, S. G.; Hyeon, T. Formation Mechanisms of Uniform Nanocrystals via Hot-Injection and Heat-Up Methods. *Small* **2011**, *7* (19), 2685−2702.

(41) Xia, Y.; Xiong, Y.; Lim, B.; Skrabalak, S. E. Shape-Controlled Synthesis of Metal Nanocrystals: Simple Chemistry Meets Complex Physics? *Angew. Chem., Int. Ed.* **2009**, *48* (1), 60−103.

(42) Kwon, S. G.; Piao, Y.; Park, J.; Angappane, S.; Jo, Y.; Hwang, N.-M.; Park, J.-G.; Hyeon, T. Kinetics of Monodisperse Iron Oxide Nanocrystal Formation by "Heating-up" Process. *J. Am. Chem. Soc.* **2007**, *129* (41), 12571−12584.

(43) Hyeon, T.; Lee, S. S.; Park, J.; Chung, Y.; Na, H. B. Synthesis of Highly Crystalline and Monodisperse Maghemite Nanocrystallites without a Size-Selection Process. *J. Am. Chem. Soc.* **2001**, *123* (51), 12798−12801.

(44) Bronstein, L. M.; Huang, X.; Retrum, J.; Schmucker, A.; Pink, M.; Stein, B. D.; Dragnea, B. Influence of Iron Oleate Complex Structure on Iron Oxide Nanoparticle Formation. *Chem. Mater.* **2007**, *19* (15), 3624−3632.

(45) Baaziz, W.; Pichon, B. P.; Lefevre, C.; Ulhaq-Bouillet, C.; Greneche, J.-M.; Toumi, M.; Mhiri, T.; Bégin-Colin, S. High Exchange Bias in Fe3−δO4@CoO Core Shell Nanoparticles Synthesized by a One-Pot Seed-Mediated Growth Method. *J. Phys. Chem. C* **2013**, *117* (21), 11436−11443.

(46) Hufschmid, R.; Arami, H.; Ferguson, R. M.; Gonzales, M.; Teeman, E.; Brush, L. N.; Browning, N. D.; Krishnan, K. M. Synthesis of Phase-Pure and Monodisperse Iron Oxide Nanoparticles by Thermal Decomposition. *Nanoscale* **2015**, *7* (25), 11142−11154.

(47) Herman, D. A. J.; Cheong-Tilley, S.; McGrath, A. J.; McVey, B. F. P.; Lein, M.; Tilley, R. D. How to Choose a Precursor for Decomposition Solution-Phase Synthesis: The Case of Iron Nano-particles. *Nanoscale* **2015**, *7* (14), 5951−5954.

(48) Sharifi Dehsari, H.; Heidari, M.; Halda Ribeiro, A.; Tremel, W.; Jakob, G.; Donadio, D.; Potestio, R.; Asadi, K. Combined Experimental and Theoretical Investigation of Heating Rate on Growth of Iron Oxide Nanoparticles. *Chem. Mater.* **2017**, *29* (22), 9648−9656.

(49) Özdamar, B.; Bouzid, A.; Ori, G.; Massobrio, C.; Boero, M. First-Principles Study of Dissociation Processes for the Synthesis of Fe and Co Oxide Nanoparticles. *J. Chem. Theory Comput.* **2018**, *14* (1), 225−235.

(50) Rodríguez-Carvajal, J. Recent Advances in Magnetic Structure Determination by Neutron Powder Diffraction. *Phys. B* **1993**, *192* (1), 55−69.

(51) Le Bail, A.; Duroy, H.; Fourquet, J. L. Ab Initio Structure Determination of LiSbWO6 by X Ray Powder Diffraction. *Mater. Res. Bull.* **1988**, *23*, 447−452.

(52) Car, R.; Parrinello, M. Unified Approach for Molecular Dynamics and Density-Functional Theory. *Phys. Rev. Lett.* **1985**, *55* (22), 2471−2474.

(53) Kohn, W.; Sham, L. J. Self-Consistent Equations Including Exchange and Correlation Effects. *Phys. Rev.* **1965**, *140* (4A), A1133−A1138.

(54) *CPMD, Copyright IBM Corp. 1990−2018, Copyright MPI Für Festkörperforschung Stuttgart 1997−2001.*

(55) Becke, A. D. Density-Functional Exchange-Energy Approx-imation with Correct Asymptotic Behavior. *Phys. Rev. A: At., Mol., Opt. Phys.* **1988**, *38* (6), 3098−3100.

(56) Lee, C.; Yang, W.; Parr, R. G. Development of the Colle-Salvetti Correlation-Energy Formula into a Functional of the Electron Density. *Phys. Rev. B: Condens. Matter Mater. Phys.* **1988**, *37* (2), 785−789.

(57) Troullier, N.; Martins, J. L. Efficient Pseudopotentials for Plane-Wave Calculations. *Phys. Rev. B: Condens. Matter Mater. Phys.* **1991**, *43* (3), 1993−2006.

(58) Goedecker, S.; Teter, M.; Hutter, J. Separable Dual-Space Gaussian Pseudopotentials. *Phys. Rev. B: Condens. Matter Mater. Phys.* **1996**, *54* (3), 1703−1710.

(59) Grimme, S. Semiempirical GGA-Type Density Functional Constructed with a Long-Range Dispersion Correction. *J. Comput. Chem.* **2006**, *27* (15), 1787−1799.

(60) Yang, F.; Massobrio, C.; Boero, M. Tuning Magnetic Properties with Pressure in Hybrid Organic−Inorganic Materials: The Case of Copper Hydroxide Acetate. *J. Phys. Chem. C* **2014**, *118* (32), 18700−18705.

(61) Chaker, Z.; Ori, G.; Boero, M.; Massobrio, C. The Role of 2D/3D Spin-Polarization Interactions in Hybrid Copper Hydroxide Acetate: New Insights from First-Principles Molecular Dynamics. *Beilstein J. Nanotechnol.* **2017**, *8*, 857−860.

(62) Evrard, Q.; Chaker, Z.; Roger, M.; Sevrain, C. M.; Delahaye, E.; Gallart, M.; Gilliot, P.; Leuvrey, C.; Rueff, J.-M.; Rabu, P.; Massobrio, C.; Boero, M.; Pautrat, A.; Jaffrès, P.-A.; Ori, G.; Rogez, G. Layered Simple Hydroxides Functionalized by Fluorene-Phosphonic Acids: Synthesis, Interface Theoretical Insights, and Magnetoelectric Effect. *Adv. Funct. Mater.* **2017**, *27* (41), 1703576.

(63) Sprik, M.; Ciccotti, G. Free Energy from Constrained Molecular Dynamics. *J. Chem. Phys.* **1998**, *109* (18), 7737−7744.

(64) Boero, M.; Parrinello, M.; Terakura, K. First Principles Molecular Dynamics Study of Ziegler−Natta Heterogeneous Catalysis. *J. Am. Chem. Soc.* **1998**, *120* (12), 2746−2752.

(65) Boero, M.; Morikawa, Y.; Terakura, K.; Ozeki, M. First Principles Study of Thermal Decomposition of Alkyl-Gallium and Tertiary Butylarsine. *J. Chem. Phys.* **2000**, *112*, 9549−9556.

(66) Nelson, P. N.; Taylor, R. A. Theories and Experimental Investigations of the Structural and Thermotropic Mesomorphic Phase Behaviors of Metal Carboxylates. *Appl. Petrochem. Res.* **2014**, *4* (3), 253−285.

(67) Akanni, M. S.; Okoh, E. K.; Burrows, H. D.; Ellis, H. A. The Thermal Behaviour of Divalent and Higher Valent Metal Soaps: A Review. *Thermochim. Acta* **1992**, *208*, 1−41.

(68) Santoyo Salazar, J.; Perez, L.; de Abril, O.; Truong Phuoc, L.; Ihiawakrim, D.; Vazquez, M.; Greneche, J.-M.; Begin-Colin, S.; Pourroy, G. Magnetic Iron Oxide Nanoparticles in 10−40 Nm Range: Composition in Terms of Magnetite/Maghemite Ratio and Effect on the Magnetic Properties. *Chem. Mater.* **2011**, *23* (6), 1379−1386.

(69) Liu, X.; Pichon, B. P.; Ulhaq, C.; Lefèvre, C.; Grenèche, J.-M.; Bégin, D.; Bégin-Colin, S. Systematic Study of Exchange Coupling in Core−Shell Fe3−δO4@CoO Nanoparticles. *Chem. Mater.* **2015**, *27* (11), 4073−4081.

(70) Henkelman, G.; Arnaldsson, A.; Jónsson, H. A Fast and Robust Algorithm for Bader Decomposition of Charge Density. *Comput. Mater. Sci.* **2006**, *36* (3), 354−360.

(71) Boero, M.; Ikeshoji, T.; Terakura, K. Density and Temperature Dependence of Proton Diffusion in Water: A First-Principles Molecular Dynamics Study. *ChemPhysChem* **2005**, *6* (9), 1775−1779.

(72) Pérez, N.; López-Calahorra, F.; Labarta, A.; Batlle, X. Reduction of Iron by Decarboxylation in the Formation of Magnetite Nanoparticles. *Phys. Chem. Chem. Phys.* **2011**, *13* (43), 19485−19489.

(73) Mahieu, N.; Canet, D.; Cases, J. M.; Boubel, J. C. Micellization of Sodium Oleate in Water-D2 as Probed by Proton Longitudinal Magnetic Relaxation and Self-Diffusion Measurements. *J. Phys. Chem.* **1991**, *95* (4), 1844−1846.